Dynamics of Pulsing Flow in Trickle Beds

A macroscopic model of two-phase flow in packed beds, based on the volume-averaged equations of motion for the gas and liquid phases, was analyzed in an attempt to understand the onset and evolution of fully-developed pulsing flow in trickle beds. By assuming that solutions take the form of waves travelling at constant speed, periodic solutions to these equations are found which can be associated with long-time, asymptotic behavior of pulses in a very long bed. Families of one-dimensional waves which exist at a particular set of mass fluxes can be characterized by infinite period bifurcations in the travelling wave frame. We numerically follow these bifurcations as the fluxes are changed, generating bifurcation diagrams for the original model. The results predict that properties of one-dimensional pulses should correlate with the total superficial velocity through the bed. A hysteresis in the trickling-pulsing transition is also predicted.

David C. Dankworth
I. G. Kevrekidis
S. Sundaresan
Department of Chemical Engineering
Princeton University
Princeton, NJ 08544

Introduction

Trickle beds are used widely in the chemical and petroleum industries for contacting and/or reaction of gas and liquid phases. Although the most general definition would include countercurrent flow and cocurrent upflow, a trickle bed is usually encountered as gas and liquid flowing cocurrently downward through a packed bed. Major processes carried out in trickle beds include hydrocracking, hydrodesulphurization, and oxidation reactions.[1]

Pulsing flow arises in trickle beds at relatively high gas and liquid throughput. Pulsing flow is characterized by alternating regions of high and low liquid holdup which spontaneously form and propagate down the bed (Beimesch and Kessler, 1971; Weekman and Myers, 1964; Christensen et al., 1986). A number of industrial reactors operate near the trickling-to-pulsing transition (Satterfield, 1975). The nature of two-phase flow in the trickling regime is very different from that in the pulsing regime. Hence, it is of fundamental importance in the design and scale-up of trickle-bed reactors to formulate mathematical models for the hydrodynamics which can describe both the uniform flow at low throughput and the time-dependent flow at high throughput, as well as indicating when the transition between these two flows will happen. The approaches to hydrodynamic modeling can be classified into two groups: the microscopic approach and the macroscopic approach.

Correspondence concerning this paper should be addressed to S. Sundaresan.

The microscopic approach involves examination of processes which occur at the single-pore level. Analogies are drawn between flooding in two-phase pipe flow and the trickling-pulsing transition in a packed bed. Similar analogies can be made to identify transitions between other flow regimes. Ng (1986) and Melli (1989) have adopted this approach and achieved mixed success. The connection between behavior in a single pore and the behavior of a large collection of pores is not obvious, however, especially for the case of time-dependent flows.

Instead of considering only the detailed behavior at the particle scale, macroscopic models are formulated in terms of average properties over a volume larger than a single particle (Saez and Carbonell, 1985; Sundaresan, 1987; Grosser et al., 1988). This type of model treats the two fluid phases as separate, interpenetrating continua. Grosser et al. (1988) have demonstrated that such a macroscopic model yields a steady uniform flow at low throughputs, which is identified as trickling flow. Upon increasing the throughputs, a loss of stability of this uniform state occurs which is identified as the trickling-to-pulsing transition. Their study was restricted to a linear stability analysis of the uniform state, and no attempt was made to follow the solution structure which evolves after the loss of stability.

The objective of the present study is to analyze the nonlinear behavior of the two-phase flow in packed beds, as predicted by such a macroscopic model, at conditions where the uniform state is unstable. The motivation for such a study is twofold: 1. understanding the evolution of pulsing flow and its details is important, as such flow conditions are indeed encountered in engineering practice; 2. a wealth of data on the details of pulsing in pilot-scale units are available in the literature. Hence, the model predictions can be readily compared with available data. Such a comparison is perhaps a very stringent test of the model. Such a model validation is essential, given the empirical inputs that are embodied in it, before it can be used with confidence in exploring scale-up and in next-generation reactor models.

Model

Equations of motion

For a uniformly packed column of porosity ϵ, if both of the phases are assumed to be incompressible, the continuity and momentum balances in terms of the volume fraction occupied by each phase and the local mean velocities can be written as:

Volume:

$$\epsilon_l + \epsilon_g = \epsilon \tag{1}$$

Continuity:

$$\frac{\partial \epsilon_i}{\partial t} + \nabla \cdot (\epsilon_i \underline{u}_i) = 0, \qquad i = l, g \tag{2}$$

Momentum:

$$\rho_i \epsilon_i \left[\frac{\partial \underline{u}_i}{\partial t} + \underline{u}_i \cdot \nabla \underline{u}_i \right] = -\epsilon_i \nabla pi + \epsilon_i \rho_i g + \underline{F}_i + \nabla \cdot [\epsilon_i \underline{\underline{\tau}}_i + \epsilon_i \underline{\underline{R}}_i], \; i = l, g \tag{3}$$

Interfacial drag forces

The $\underline{F}_i$ terms in Eq. 3 represent the volume-averaged forces exerted on one phase by the other phases across their interfaces. If the packaging is completely wetted, the gas-phase drag only will have contributions due to contact with the liquid phase. The liquid phase, however, will experience forces from both the gas and the solid. These drag forces are very large in magnitude and tend to dominate the momentum balance equations. There is no obvious way to relate these forces to the mean properties of the flow through first principles, making it necessary to use semiempirical constitutive relations for these terms. Such relations have been developed from experimental measurements by Saez and Carbonell (1985) and were used by Grosser et al. (1988) in the initial analysis of the model. Those relations are intended to correspond to the hydrodynamic properties of bicontinuous trickling flow. In our study, we have modified the correlations slightly.

$$\underline{F}_g = -\left\{ \frac{A \mu_g (1-\epsilon)^2 \epsilon^{1.8}}{d_e^2 \epsilon_g^{2.8}} + \frac{B \rho_g (1-\epsilon) \epsilon^{1.8}}{d_e \epsilon_g^{1.8}} |\underline{u}_g - \underline{u}_l| \right\} (\underline{u}_g - \underline{u}_l) \tag{4}$$

$$\underline{F}_l = -\left\{ \frac{\epsilon - \epsilon_l^r}{\epsilon_l - \epsilon_l^r} \right\}^{2.43} \left\{ \frac{A \mu_l (1-\epsilon)^2 \epsilon_l^2}{d_e^2 \epsilon^3} + \frac{B \rho_l (1-\epsilon) \epsilon_l^3}{d_e \epsilon^3} |\underline{u}_l| \right\} \underline{u}_l - \underline{F}_g \tag{5}$$

The drag on the gas phase is now expressed in terms of the relative velocity of the two phases with respect to each other. Also, the liquid drag relation now contains two terms, one for the liquid-solid interactions and one for the gas-liquid interactions. It is trivial to show that these changes do not greatly affect the model predictions in trickling flow, since the gas velocity is much greater than the liquid velocity and the drag forces on the liquid are much larger than those on the gas. When the liquid velocity becomes significant, however, the gas experiences less drag.

Saez and Carbonell (1985) correlated the residual liquid holdup at zero flow in Eq. 5 as:

$$\epsilon_l^r = \frac{1}{20 + 0.9\, E\ddot{o}} \tag{6}$$

where the Eötvos number is given by

$$E\ddot{o} = \frac{\rho_l g d_e^2 \epsilon^2}{\sigma (1-\epsilon)^2} \tag{7}$$

Capillary pressure

Grosser et al. (1988) proposed that the difference in the liquid-phase and gas-phase pressures, i.e., the capillary pressure, may be represented by the J-function correlation of Leverett (1941):

$$p_c = p_g - p_l = \left[\frac{\epsilon}{k} \right]^{1/2} \sigma J(s_l) \tag{8}$$

where $s = \epsilon/\epsilon$. The basis for expecting this to be a reliable first approximation has also been discussed by them.

The J-function is dependent on the liquid saturation and on the flow history of the bed. Grosser et al. (1988) used the J-function corresponding to drainage in their determination of stability transitions. We will use the same curve here, which can be expressed mathematically by the following expression.

$$J(s_l) = 0.48 + 0.036 \ln \left[\frac{l - s_l}{s_l} \right] \tag{9}$$

Stress terms

Grosser et al. (1988) ignored the viscous and pseudoturbulence stresses in their linear stability analysis and argued that these terms should have negligible effect on the location of the trickling-to-pulsing transition. While this assumption is indeed correct, it will be seen later that these terms are essential to render the problem well-posed in the interior of the pulsing regime. Lumping the viscous and pseudoturbulence stresses together into a single stress tensor. $\underline{\underline{E}}$ gives

$$\underline{\underline{E}}_i = \underline{\underline{\tau}}_i + \underline{\underline{R}}_i. \tag{10}$$

A suitable constitutive relation must be used to approximate the combined stress tensor in terms of mean velocities and volume fractions. Following the example of Anderson and Jackson (1968), we will consider a simple Newtonian form, where the stress is directly proportional to the rate of deformation:

$$\underline{\underline{E}}_i = \lambda_i^* (\nabla \cdot \underline{u}_i) I + \mu_i^* [\nabla \underline{u}_i + (\nabla \underline{u}_i)^T - 2/3 (\nabla \cdot \underline{u}_i) I], i = l, g \quad (11)$$

where the parameters λ_i^* and μ_i^* are the "effective" bulk and shear viscosities of the ith phase. In general, effective viscosities will depend on the flow conditions.

If we restrict our attention to unidirectional flow along the z-axis, with no gradients in the transverse directions, the divergence of the deviatoric stress reduces to the simpler expression:

$$\epsilon_i E_{iz} = \frac{d}{dz}\left(\bar{\mu}_i \epsilon_i \frac{du_{iz}}{dz}\right) \quad (12)$$

where the effective viscosity is now a combination of the bulk and shear terms:

$$\bar{\mu}_i = \lambda_i^* + \frac{4}{3}\mu_i^* \quad (13)$$

It is neither easy to determine the effective viscosity parameter from first principles nor measure it experimentally. However, it can be readily shown that

$$\bar{\mu}_i \sim \rho_i u_i d_e. \quad (14)$$

This scaling suggests that the effective viscosity should be on the order of 0.1 kg/m · s for water and 0.0001 kg/m · s for air in a bed of 3-mm-diameter spheres. In the remainder of this paper, we will use the above value for the liquid-phase effective viscosity and will neglect the gas-phase contribution. The model predictions are relatively insensitive to the values of the effective viscosities, as they indeed should be!

One-Dimensional Model

The full vector equations of motion (Eqs. 1–3) are very complicated to analyze, while much useful information can be derived from a simpler, one-dimensional model. If we assume that the velocities and volume fractions are uniform in the lateral directions and that all variations take place in the axial direction, parallel to gravity, the following one-dimensional version of the equations can be written:

$$\frac{\partial \epsilon_i}{\partial t} + \frac{\partial \epsilon_i u_{iz}}{\partial z} = 0, \qquad i = l, g \quad (15)$$

$$\rho_i \epsilon_i \left[\frac{\partial u_{iz}}{\partial t} + u_{iz}\frac{\partial u_{iz}}{\partial z}\right] = -\epsilon_i \frac{\partial p_i}{\partial z} + \epsilon_i \rho_i g + F_{iz} + \frac{\partial}{\partial z}\left[\epsilon_i \bar{\mu}_i \frac{\partial u_{iz}}{\partial z}\right], \qquad i = l, g \quad (16)$$

To model a bed of finite length, suitable boundary conditions would have to be included to make the model well posed. In the analysis which follows, we will consider a bed which extends to infinity in all directions. In such a bed, there is only the condition that the velocities, volume fractions, and pressure gradients be bounded everywhere.

The one-dimenstional continuity equations given by Eq. 15 can be combined with Eq. 1 and integrated to produce a relation between the volumetric flux of the phases at every point:

$$u_l \epsilon_l + u_g \epsilon_g = U_T \quad (17)$$

U_T is a constant which represents the combined average superficial velocity of both phases. This can be expressed in terms of the mass fluxes, L and G, of each phase as in Eq. 18.

$$U_T = \frac{L}{\rho_l} + \frac{G}{\rho_g} \quad (18)$$

Stability in the 1-D equations

Before examining the time-dependent behavior of the model, we should first discuss the stability of the uniform steady-flow solution in the 1-D (one-dimensional) model. Grosser et al. (1988) presented such a stability analysis for the 1-D model without stress terms and showed that the uniform state can lose stability as the external mass fluxes are increased. As shown below, the stress terms introduce a dependence of the stability on the wave number of the imposed perturbation and render the model well-posed. This is due to a dissipation of very high-frequency perturbations which is not possible without inclusion of stress terms in the model.

For the 1-D model, the uniform state is obtained when

$$\frac{F_l^o}{\epsilon_l^o} - \frac{F_g^o}{\epsilon_g^o} + g(\rho_l - \rho_g) = 0 \quad (19)$$

where externally imposed mass fluxes of the two phases are defined as

$$L = \rho_l \epsilon_l^o u_l^o, \qquad G = \rho_g \epsilon_g^o u_g^o \quad (20)$$

In the analysis, dependent variables are expressed in terms of perturbations from the uniform state. The drag force terms are linearized by expanding in a Taylor series and keeping only the terms in the perturbations as follows:

$$F_i = F_i^o + u_l^* \alpha_{il} + u_g^* \alpha_{ig} + \epsilon_i^* \beta_i \quad (21)$$

where the first derivatives of the drag force evaluated at the uniform solution are given by

$$\alpha_{ij} = \left[\frac{dF_i}{du_j}\right]^o; \beta_i = \left[\frac{dF_i}{d\epsilon_i}\right]^o, i, j = l, g \quad (22)$$

After similar linearization of the full model equations a general solution can be postulated for an initial sinusoidal disturbance as

$$y = \hat{y} \exp(\chi t + j\omega z) \quad (23)$$

where ω is the wave number of the perturbation and χ is the complex wave velocity which is to be determined. Substitution of Eq. 23 into the linearized equations gives a polynomial in χ and ω. This polynomial (Eq. 24) can be solved for the real and imaginary parts of χ in terms of the wave number and several coefficients (W_i) which depend only on the mass fluxes and the fluid and bed properties.

$$\chi^2 W_l + \chi [W_2 + \omega^2 W_6 + 2j\omega W_3] - \omega^2 W_4 - j(\omega W_5 - \omega^3 W_7) = 0 \quad (24)$$

$$W_1 = \frac{\rho_g}{\epsilon_g^o} + \frac{\rho_l}{\epsilon_l^o} \quad (25)$$

$$W_2 = -\left[\frac{\alpha_g}{\epsilon_g^{o^2}} + \frac{\alpha_l}{\epsilon_l^{o^2}}\right] + \left[\frac{\alpha_{lg} + \alpha_{gl}}{\epsilon_l^o \epsilon_g^o}\right] \quad (26)$$

$$W_3 = \frac{\rho_g u_g^o}{\epsilon_g^o} + \frac{\rho_l u_l^o}{\epsilon_l^o} \quad (27)$$

$$W_4 = \frac{\rho_g u_g^{o^2}}{\epsilon_g^o} + \frac{\rho_l u_l^{o^2}}{\epsilon_l^o} + \left[\frac{\epsilon}{k}\right]^{1/2} \sigma J'(\epsilon_l^o) \quad (28)$$

$$W_5 = \frac{F_g}{\epsilon_g^{o^2}} + \frac{F_l}{\epsilon_l^{o^2}} - \frac{\beta_l}{\epsilon_l^o} - \frac{\beta_g}{\epsilon_g^o} + \frac{\alpha_l u_l^o}{\epsilon_l^{o^2}} + \frac{\alpha_g u_g^o}{\epsilon_g^{o^2}} - \frac{\alpha_{lg} u_g^o + \alpha_{gl} u_l^o}{\epsilon_l^o \epsilon_g^o} \quad (29)$$

$$W_6 = \frac{\bar{\mu}_g}{\epsilon_g^o} + \frac{\bar{\mu}_l}{\epsilon_l^o} \quad (30)$$

$$W_7 = \frac{\bar{\mu}_g u_g^o}{\epsilon_g^o} + \frac{\bar{\mu}_l u_l^o}{\epsilon_l^o} \quad (31)$$

where

$$J'(\epsilon_l^o) = \left[\frac{dJ}{d\epsilon_l}\right]^o \quad (32)$$

If we split up the complex wave velocity into its real and imaginary parts,

$$\chi = \xi + j\omega v \quad (33)$$

the real part indicates the growth rate of a disturbance, while the imaginary part is related to the speed at which a disturbance would propagate down the bed.

An algebraic criterion for stability can be derived by requiring the growth rate, ξ, to be negative:

$$C_1 - 2\omega^2 C_2 + \omega^4 C_3 < 0 \quad (34)$$

where the C coefficients depend only on the W coefficients Eqs. 25–31:

$$C_1 = W_1 W_5^2 + 2W_3 W_2 W_5 + W_2^2 W_4 \quad (35)$$

$$C_2 = W_7 (W_1 W_5 + W_2 W_3) - W_6 (W_3 W_5 + W_2 W_4) \quad (36)$$

$$C_3 = W_1 W_7^2 - 2W_3 W_6 W_7 + W_6^2 W_4 \quad (37)$$

If the effective viscosities are zero, the above stability criterion becomes the same as that derived by Grosser et al (1988):

$$C_1 < 0 \quad (38)$$

and this is valid for all wavenumbers. An unstable uniform solution is one for which a positive growth rate is obtained for some wavenumbers. Hence, it is important to consider the wavenumber dependence of ξ. If effective viscosities are set equal to zero, as was done by Grosser et al. (1988), then it can be readily shown that $\xi(\omega) > 0$ for all ω, when Eq. 38 is violated. Furthermore, the growth rate increases monotonically as ω increases, and $\xi \longrightarrow \infty$ as $\omega \longrightarrow \infty$. A dynamic model manifesting such a character is said to be ill-posed, and no meaningful dynamic solution can be extracted from it under unstable conditions. Also, such a dynamic model is physically incorrect. However, when one or both of the effective viscosities are nonzero, the dependence of the growth rate on ω is modified considerably. This is illustrated in Figure 1, which shows the growth rate, ξ, plotted against the wave number ω for the several flow conditions at fixed values of gas and liquid effective viscosities. Thus there exists a critical wavenumber for given operating conditions above which ξ is negative. Such a feature renders the dynamic problem well-posed and meaningful to analyze.

An often-used practice is to presume that the wavenumber for which the growth rate ξ of the linear waves has the largest positive value will prevail and use this criterion to extract certain model parameters from experimental data. This, for example,

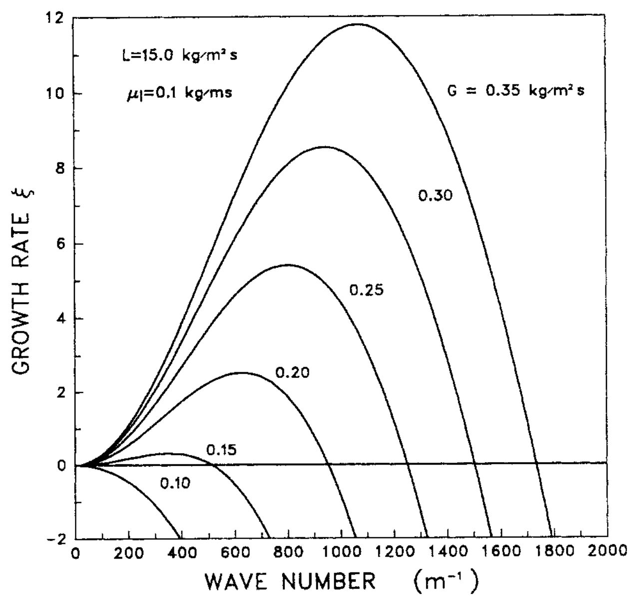

Figure 1. Wave-number-dependent perturbation growth rates.

Growth rate curves for $L = 15$ kg/m² · s and several gas mass fluxes.

has been done in the context of periodic waves in liquid-fluidized beds (Homsy et al., 1980). Such an approach in the present context, using experimental data on pulse frequencies to deduce effective viscosities, resulted in a physically unsupportable estimate for $\underline{\mu}_l$ of 1,000 poise (100 Pa · s), exposing the fallacy in such a procedure.

Traveling Wave Analysis

While it is possible to numerically examine general solutions to the partial differential equations of the 1-D model, it is not necessary to integrate the full equations to extract useful information about the existence of asymptotic, time-dependent solutions. Fully-developed pulsing is observed to be more or less regular, and the variations in holdup and velocity during pulsing are roughly periodic. This suggests that we look for periodic solutions of the equations in an infinite bed.

If we assume that fully-developed waves will travel through the bed at constant velocity, we can make a change of variables to a moving coordinate x which is related to both time and position by

$$x = \frac{z - ct}{\lambda} \tag{39}$$

Under this change of variables, the partial derivatives in time and space become total derivatives in x. The new coordinate is scaled on a characteristic length, λ, which will take on physical meaning as a wavelength when we calculate periodic solutions.

Continuity and velocity

The continuity equations (Eqs. 15) become

$$- c\frac{d\epsilon_i}{dx} + \frac{du_i\,\epsilon_i}{dx} = 0, \tag{40}$$

which can be integrated to yield algebraic relations among the velocity, the volume fraction, and the wave speed:

$$\epsilon_i\,(u_i - c) = k_i, \qquad i = l, g \tag{41}$$

where k_i (henceforth, referred to as relative flux of phase i) is constant and can be interpreted as the superficial velocity of phase i relative to the traveling reference frame. This reflects the fact that flow of each phase should be constant when observed from a reference frame traveling with the wave velocity, c. Equation 41 can be combined with Eq. 17 to obtain a relation between the relative superficial velocities of the two phases and the total superficial velocity:

$$k_l + k_g = U_T - \epsilon c. \tag{42}$$

As a consequence of the conservation of mass flux relative to a traveling wave given by Eq. 41, the interstitial velocities become completely determined by the liquid saturation, s, and the parameters k_i and c.

$$u_l = c + \frac{k_l}{\epsilon s} \tag{43}$$

$$u_g = c + \frac{k_g}{\epsilon(1 - s)} \tag{44}$$

Traveling Wave Equation

The momentum equations (Eqs. 16) can be similarly transformed to the traveling coordinates. By using Eqs. 43 and 44 to eliminate the velocities, the transformed equations can be combined to yield a single second-order ordinary differential equation for the variation of liquid saturation:

$$\overline{W}_7\frac{d^2s}{dx^2} - \lambda\,\overline{W}_4\frac{ds}{dx} + A_1\left(\frac{ds}{dx}\right)^2 = \frac{\lambda^2}{\epsilon}F \tag{45}$$

where the coefficients $\overline{W}_7$, $\overline{W}_4$, A_l and F are functions of saturation and of the parameters as follows:

$$\overline{W}_4 = \frac{\rho_g k_g^2}{\epsilon_g^3} + \frac{\rho_l k_l^2}{\epsilon_l^3} + \frac{dp_c}{d\epsilon_l} \tag{46}$$

$$\overline{W}_7 = \frac{\overline{\mu}_g k_g}{\epsilon_g^2} + \frac{\overline{\mu}_l k_l}{\epsilon_l^2} \tag{47}$$

$$A_l = \frac{\overline{\mu}_g k_g}{\epsilon_g^3} - \frac{\overline{\mu}_l k_l}{\epsilon_l^3} \tag{48}$$

$$F = \frac{F_l}{\epsilon_l} - \frac{F_g}{\epsilon_g} + g\,(\rho_l - \rho_g) \tag{49}$$

A uniform flow solution of equations (Eqs. 15 and 16) is obtained when

$$\frac{ds}{dx} = 0 \tag{50}$$

and

$$F = 0 \tag{51}$$

Bifurcations of steady flow in the traveling frame

A bifurcation analysis in the traveling wave frame of the uniform steady flow solution provides valuable insight into the evolution of fully-developed, periodic, traveling wave solutions. Although the bifurcations of the traveling wave equation also affect the stability of solutions in that frame, this stability is unrelated to stability of uniform solutions in the full 1-D model. Bifurcations do correspond to important phenomena in the 1-D model, however, as shown in the analysis below.

The external mass fluxes corresponding to a particular uniform steady-flow solution are specified through the k_l and k_g parameters. From Eq. 41:

$$k_l = \frac{L}{\rho_l} - c\,\epsilon_l^o \tag{52}$$

$$k_g = \frac{G}{\rho_g} - c\,\epsilon_g^o. \tag{53}$$

For given relative fluxes k_l and k_g, a fixed point $s^o = \epsilon_l^0/\epsilon$ corresonding to $F\,(k_l, k_g, c, s^o) = 0$ will correspond to external mass fluxes L and G.

The linearized form of the traveling wave equation can be derived by expressing the liquid volume fraction as

$$e = \epsilon_l - \epsilon_l^o \tag{54}$$

and substituting Eqs. 52–54 into Eq. 45 to obtain

$$\overline{W}_7^o e'' = \overline{W}_4^o e' + \left(\frac{dF}{d\epsilon_l}\right)^o e, \tag{55}$$

where the length scale, λ, has been set to one. The three coefficients of the linearized equation (Eq. 55) are now constants, and they are all related directly to coefficients W_l to W_7 from the 1-D model analysis:

$$\overline{W}_7^o = W_7 - W_6 c \tag{56}$$

$$\overline{W}_4^o = W_4 - 2\,c\,W_3 + c^2\,W_1 \tag{57}$$

$$\left(\frac{dF}{d\epsilon_l}\right)^o = -\,W_5 - c\,W_2. \tag{58}$$

A general solution of the linearized equation will have the form of an exponential such as

$$e = \hat{e}\exp(\chi\,x), \tag{59}$$

where χ is a complex growth rate. χ can also be interpreted as an eigenvalue of the Jacobian of the traveling wave equation at a particular fixed point corresponding to uniform flow at a specified c, L, and G. Introducing Eq. 59 into the linearized traveling wave equation produces a polynomial in c and χ. Solving this polynomial for χ gives two solutions:

$$\chi = \frac{\overline{W}_4^o \pm \sqrt{\overline{W}_4^{o2} - 4\,\overline{W}_7^o(W_5 + cW_2)}}{2\,\overline{W}_7^o} \tag{60}$$

Changes in stability occur when the real parts of one or both of these eigenvalues vanish. For given external flow rates, eigenvalues depend only on the wave speed, c. The analysis presented here is nothing more than a reformulation of the stability analysis for the 1-D model described earlier. Here the wave speed is the explicit parameter and wave number is implicitly specified by the imaginary part of χ, while in the 1-D analysis the wave number is the explicit parameter and the propagation speed is given implicitly by the imaginary part of the growth rate.

The traveling wave equation (Eq. 45) is a second-order ODE, which can be written as a two-dimensional dynamical system of two first-order ODE's. For such a two-dimensional system, we generically expect two types of steady-state bifurcations: limit points and Hopf bifurcations. At limit points, a single real eigenvalue changes sign, while a Hopf bifurcation occurs when the real part of a pair of complex eigenvalues changes sign. We will be particularly interested in the Hopf bifurcations, as they signal the birth of periodic solutions. The conditions for a Hopf bifurcation in the traveling wave frame are:

$$\overline{W}_7^o(W_5 + cW_2) > 0 \tag{61}$$

and

$$\overline{W}_4^o = 0 \tag{62}$$

The wave speed at which a Hopf bifurcation occurs is found by solving Eq. 62 for c, which gives (where U_T and k_l are fixed)

$$c_{HB} = \frac{W_3}{W_1}\left[1 \pm \sqrt{1 - \frac{W_4\,W_1}{W_3^2}}\right]. \tag{63}$$

Note that this wave speed is not dependent on the value of the effective viscosity nor on the drag force correlations. W_3, W_4, and W_1 arise from the inertial and capillary pressure terms in the equations. The corresponding period, λ_{HB} of a limit cycle at the Hopf bifurcation is given by

$$\omega_{HB} = \frac{2\pi}{\lambda_{HB}} = \sqrt{\frac{(W_5 + c_{HB}\,W_2)}{W_7 - c_{HB}\,W_6}}. \tag{64}$$

Unlike the speed, the period depends strongly on the effective viscosities through W_6 and W_7, as well as drag forces through W_2 and W_5.

The same expressions for speed and wave number in terms of W_1 to W_7 can be derived from the analysis of the 1-D model as the critical wave number corresponding to a vanishing growth rate and its corresponding propagation velocity. *Thus, a Hopf bifurcation in the traveling wave frame with respect to the parameter c is equivalent to the stability change as wave number is decreased for the same unstable uniform solution of the 1-D model.* Similarly, the birth of limit cycles from a Hopf bifurcation corresponds to the birth of traveling wave solutions to the 1-D model.

A single real eigenvalue will vanish for any value of $\overline{W}_4^o$ when

$$c_{LP} = -\frac{W_5}{W_2}. \tag{65}$$

This speed corresponds to the propagation velocity at zero wave number in the 1-D analysis described earlier. Thus, a limit point with respect to c in the traveling wave frame is equivalent to an infinitely long wavelength perturbation in the 1-D analysis. The presence of limit points in the traveling wave model indicates that multiple steady states will occur in that frame.

The critical wave number decreases as the flux of one phase is decreased (See Figure 1) and becomes zero as the flux is decreased into the region of stable uniform flow. *This means that the conditions for change in stability in the 1-D model will satisfy the conditions for both a Hopf bifurcation and a single eigenvalue at zero in the traveling wave model.* The eigenvalues, χ, for this special case are both zero. Such double-zero singularities have special meaning in bifurcation theory, as they signal the existence of homoclinic saddle connections (SC) in addition to Hopf bifurcations and limit points (Guckenheimer and Holmes, 1983). A homoclinic connection consists of a trajectory which starts and ends at the same saddle-type fixed point.

Periodic boundary conditions

As mentioned earlier, the pulsing flow observed in pilot-scale experiments appears to be roughly periodic. So, our objective is to seek an understanding of the evolution of fully-developed, periodic traveling wave solutions in the model. Hence, we stipulate that fully-developed solutions satisfy

$$s(0) = s(1) \tag{66}$$

$$s'(0) = s'(1) = 0, \tag{67}$$

where the second equality in Eq. 67 is added to eliminate phase-shifted identical solutions.

Parameters

In the preceding presentation of the model several parameters appear. These can be divided into two catetories.

• One category contains the physical properties of the bed and of the fluids, and the externally imposed total volumetric flux of the liquid and the gas, U_T. These parameters have direct physical meaning, and are determined by the choice of bed and fluids, and generally are not allowed to vary within a single experiment.

• A second class of parameters includes the undetermined constants which arise from the method of analysis. This class is made up of the wave speed, c, wave length, λ, and the relative fluxes, k_l and k_g. However, only one of these four parameters is truly independent, as discussed below. First, a functional relationship among three of the these parameters is given by Eq. 42. Second, it is not difficult to recognize that since the periodic solutions correspond to limit cycles of the traveling wave equation, the period of these limit cycles is not an independent parameter: i.e., there is an implicit relationship among the above four parameters which emerges as a part of the solution. Third, it should be noted that externally-imposed flow rates appear in the traveling wave equation only through the parameter U_T. Therefore, of all the possible traveling wave solutions at constant U_T, only a subset will have particular average fluxes of both liquid and gas, L and G. The relation between L and G, and U_T is given by Eq. 18, specifying L and G is equivalent to specifying L and U_T, or L/U_T and U_T. For convenience, we will use either of the latter two combinations in our analysis. In the traveling wave analysis, specification of the liquid flux L is achieved by constraining the average flux of liquid to a constant value. Furthermore, as we have periodic solutions, it is sufficient to perform this averaging over a wavelength. So,

$$\frac{L}{\rho_l} = \int_0^1 u_l \epsilon s \, dx = \int_0^1 (c\epsilon s + k_l) \, dx. \tag{68}$$

Noting that c and k_l are constant for a particular limit cycle, the above constraint can be rearranged to give a condition for the integral of the saturation over the period of a single limit cycle:

$$\int_0^1 s(x) \, dx = \frac{1}{c\epsilon}\left(\frac{L}{\rho_l} - k_l\right) \tag{69}$$

These three considerations reduce the number of undetermined parameters (in the second class alluded to above) to one (say, the wave velocity, c). This means that for given external flows, L and G, there exists a one-parameter family of traveling waves parameterized by c. For each c value in an entire interval, we can find waves with k_l given by Eq. 69 and wavelength determined from the solution of the boundary value problem.

As will become evident from the following section, it is sometimes convenient to examine a relaxed problem in which the constant average liquid flux constraint Eq. 69, is dropped in order to gain a better insight into the evolution of solutions. This would necessarily increase the number of undetermined parameters to two. In such relaxed analysis, we will choose c and k_l as free parameters, and leave U_T as the only external specification. The external fluxes of a solution of the relaxed problem can then be extracted.

Model calculations

The uniform state is a readily-calculated, special solution of the traveling wave model. As discussed in an earlier section, the Hopf bifurcation point signals the birth of periodic solutions and thus provides a convenient starting point for these calculations. Limit cycles very near the Hopf bifurcation have approximately the same flow rate as the nearby uniform state. The period and speed are also known through Eqs. 63–64. An entire family of limit cycles satisfying the above constraints can then be found by continuation in the parameter c, using standard continuation codes (e.g., AUTO 86, Doedel, 1986). Of course, such continuation will only yield solution branches which evolve smoothly from the Hopf bifurcation point. As we will dicuss later, two parameter continuations in c and k_l, relaxing the integral constraint, will allow us to locate branches which would appear isolated in one-parameter diagrams.

Constrained families of waves

For discussion, we will now consider such families of waves with constant average mass flux for total superficial velocity of 0.15 m/s and for liquid mass fluxes of 15, 30, 45 and 60 kg/m^2 · s. Bed and fluid properties are chosen to correspond to air-water flowing in a bed of 3-mm spheres, as indicated in Table 1. Each constrained family starts at the Hopf bifurcation for the corresponding uniform state and grows in amplitude as the wave speed increases away from the initial bifurcation. Figure 2 shows the maximum and minimum amplitude of the limit cycles as functions of the wave speed, c. Note that curves converge to a particular wave velocity, and maximum and minimum saturations. Curves for different values of L differ in that they approach the end point from different directions. (As shown later, this behavior is due to the close approach of the corresponding limit cycles to a double heteroclinic connection between two uniform steady solutions in the c, k_l parameter space.)

Saturation profiles and waveforms

Some of the waveforms which correspond to points along a curve of constant flux limit cycles in Figure 2 are shown in Figure 3. These waves fall along the curve for $U_T = 0.15$ m/s, $L = 15$ kg/m^2 · s with higher-amplitude waves being further

Table 1. Bed Properties Used in Simulations

$A = 180$	$\rho_g = 1.17$ kg/m^3
$B = 1.8$	$\rho_l = 1{,}000$ kg/m^3
$g = 9.8$ m/s^2	$\mu_g = 1.84 \times 10^{-5}$ kg/m · s
$\sigma = 7.15 \times 10^{-2}$ kg/s^2	$\mu_l = 10^{-3}$ kg/m · s
$\epsilon = 0.4$	$d_e = 0.003$ m
$\mu_l^* = 0.1$ kg/m · s	$\mu_g^* = 0.0$

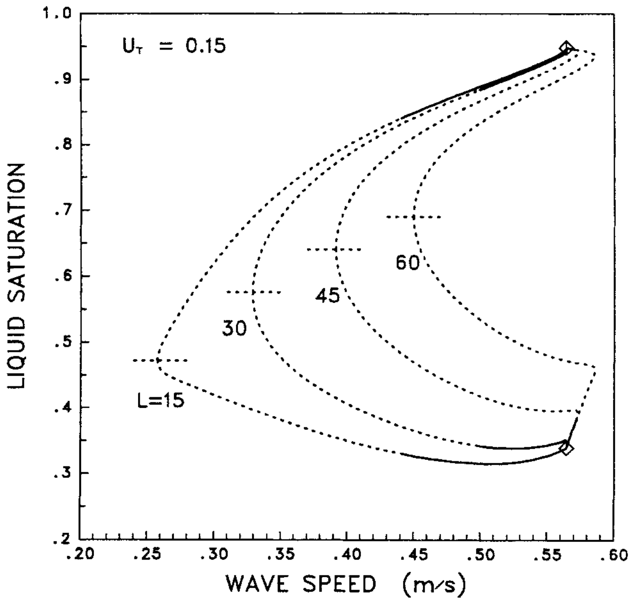

Figure 2. Constant flux traveling waves.

Four liquid fluxes shown for $U_T = 0.15$. Horizontal bar indicates uniform steady flow. Curves are minimum and maximum saturations of periodic solutions. Solid lines indicate wavelength greater than packing size.

from the Hopf bifurcation. At all points, the waves have a very wide, flat region of low saturation and a narrower, sharply varying region of high saturation. The very highest amplitude waves shown in Figure 3 correspond to points very near the heteroclinic connection. Note that the peak of the wave becomes flat and wide, as the low saturation region also becomes flatter. There is a very sharp change from one saturation level to the other, and the overall shape is that of a square wave. For this U_T, in the square-wave limit the high saturation is 97% and the low saturation is about 22%. On increasing U_T, the maximum saturation increases, and the minimum decreases.

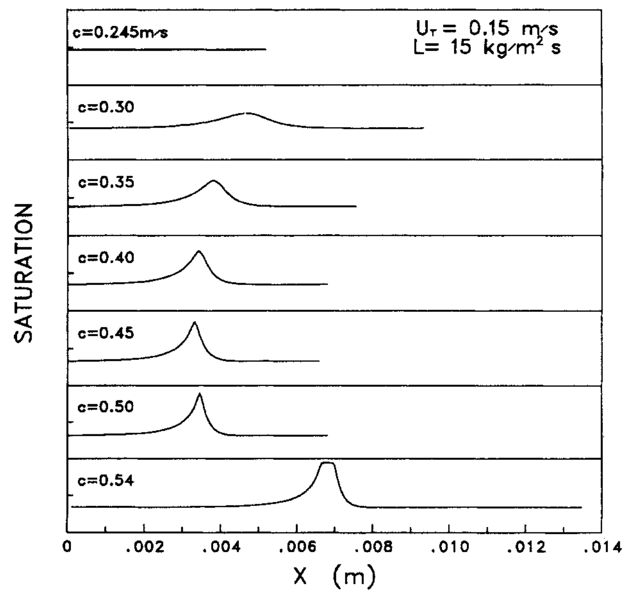

Figure 3. Wave forms *s* vs. *x*: $U_T = 0.15$, $L = 15\ kg/m^2 \cdot s$.

Periodic solutions at c = 0.24, 0.30, 0.35, 0.40, 0.45, 0.50, 0.54 m/s. Highest amplitude wave is near the double heteroclinic connection.

An interesting feature of the constrained system is that the solution branches for a fixed U_T, but various liquid-to-gas ratios always end up very near the same heteroclinic connection. *This imples that such branches end up in a square-wave shape with the same maximum and minimum saturation and wave speed regardless of the relative fluxes of gas and liquid.* Increasing the L/G ratio results in the same square waves, only with relatively broader saturation peaks. Indeed, for any ratio of liquid to gas for which the uniform steady saturation lies between the upper and lower plateau levels (denoted by ◇ in Figure 2), there will exist a high-amplitude periodic solution near this double heteroclinic connection point. The specific ratio determines the relative width of high and low plateaus.

Bifurcation analysis of relaxed problem

It will become clear later that the double heteroclinic connection possesses a special significance for the present problem. Indeed, we will show that the saturation plateaus and velocity of all physically meaningful solutions are essentially those corresponding to this special point. Therefore, we shall examine the evolution of the double heteroclinic connection more closely by study of global bifurcations in the relaxed problem (in which L is not specified). Such a study will also provide information about isolated branches of periodic solutions in the constrained problem which continuation fails to predict. The choice of the relaxed problem is quite natural, as the relaxed constraint does not influence the characteristics of the double heteroclinic connection in any way.

Here, both k_l and c are undetermined parameters, and the dynamic attractors of the traveling wave equation will change as either of these parameters is varied at constant U_T. Each of the constrained flux solutions which were discussed in the previous section will be only a part of the complete set of possible periodic solutions at a given total flux. By analyzing the bifurcation structure of the relaxed problem, it is possible to locate a well defined region in the space of parameters c and k_l which contains all of the possible limit cycle solutions of the traveling wave equation. For a second-order system, such a region will be bounded by the Hopf bifurcations at the local level and by homoclinic saddle connections on the global level.

Bifurcation diagram

The effect of changing one parameter can be easily examined by constructing a bifurcation diagram, showing the location and stability of steady states as functions of the parameter being varied. A typical bifurcation diagram is shown in Figure 4 for constant values of U_T and k_l. Uniform solutions obtained by solving Eqs. (50,51) form a single curve as c is varied, having two limit (turning) points. Depending on the value of c, it is possible to have one, two, or three uniform saturation values. The reason for the occurrence of multiple solutions in the traveling wave frame, while only a unique uniform steady state is possible for the two-phase flow problem, is discussed in Appendix A. A Hopf bifurcation may occur along the middle branch of solutions, as the real part of the eigenvalues of the linearized equation (given in Eq. 60) passes through zero along the imaginary axis. Solutions along the upper and lower branches are saddle-type unstable steady states. These evaporate (i.e.

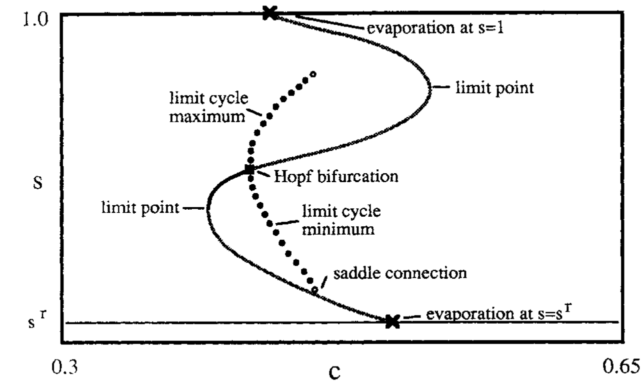

Figure 4. Bifurcation diagram for traveling wave model.

Saturation is plotted vs. wave speed. Circles indicate maximum and minimum saturation of periodic solutions. Note two limit points, Hopf bifurcation, and homoclinic connection to lower branch saddle point.

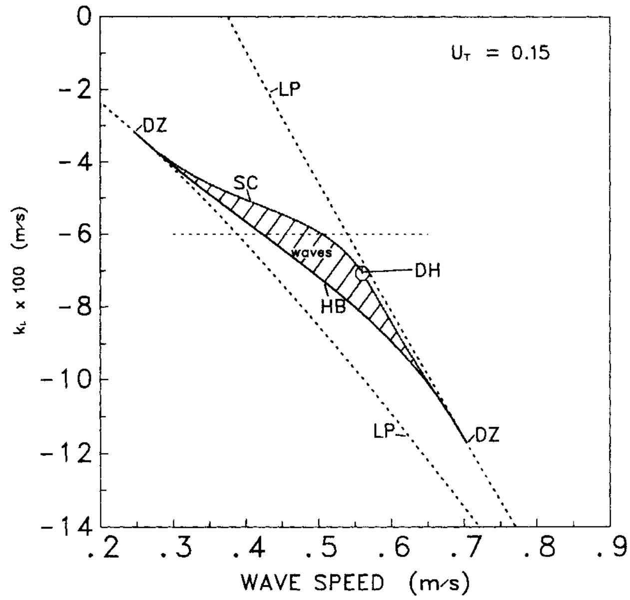

Figure 5. Two parameter diagram in c and k_l.

Limit cycles exist within the shaded region. Hopf bifurcations end at double-zero singularities at high- and low-wave speed.

disappear) as their saturation reaches either the residual saturation or unity. Starting from the Hopf bifurcation, and growing in size as wave speed increases, is a branch of periodic (limit cycle) solutions. The amplitude of the oscillations is indicated by circles marking the minimum and maximum saturation values reached by a limit cycle. As the limit cycles grow in amplitude, they eventually collide with one of the saddle-type uniform solutions on the upper or lower branches, forming a *homoclinic connection.*

If the other free parameter, k_l, is now changed, the shape of the curve and the relative positions of the bifurcations will change. As a double zero singularity is approached, both the Hopf bifurcation and the homoclinic connection will move toward one of the turning points.

Parameter space representation at constant U_T

A two parameter diagram showing the location of the bifurcation points can be used to show how the bifurcation diagram shown in Figure 4 will change as the parameter k_l is varied. Figure 5 shows such a diagram of k_l vs. c, where U_T is held constant. As shown on the figure, the two limit point curves (*LP*) are connected to the curve of Hopf bifurcations (HB) at two double-zero singularities. Limit cycles exist on one side of the Hopf bifurcations, but not on the other side. The bifurcation diagram of Figure 4 can be reproduced by following a horizontal line at constant k_l as shown. Also emanating from double-zero singularities are curves of homoclinic connections (SC), marking the disappearance of limit cycles. As the total volume flux parameter, U_T is decreased, double-zero singularities in Figure 5 move closer together. As they collide, the curve of Hopf bifurcations shrinks and disappears, along with the region of limit cycles.

Global bifurcations

Interactions of finite-amplitude periodic solutions with each other and with uniform solutions appear as global bifurcations. Usually, the result of a global bifurcation is the sudden appearance or disappearance of periodic solutions. In the parameter space representation shown in Figure 5, homoclinic connections are examples of global bifurcations. These global events themselves undergo a transition from one type to another at the double heteroclinic connection.

Solitary waves

At a homoclinic connection, the limit cycle coincides with the stable and unstable manifolds of the colliding saddle point. In other words, a trajectory in phase space which starts very close to the saddle point will return to it, as illustrated in Figure 6a. The phase space representation sketched in this figure shows a spiral fixed point (SN) and two saddle-type fixed points (SP). In the diagram, all of the free parameters (c, k_l, and U_T) are fixed

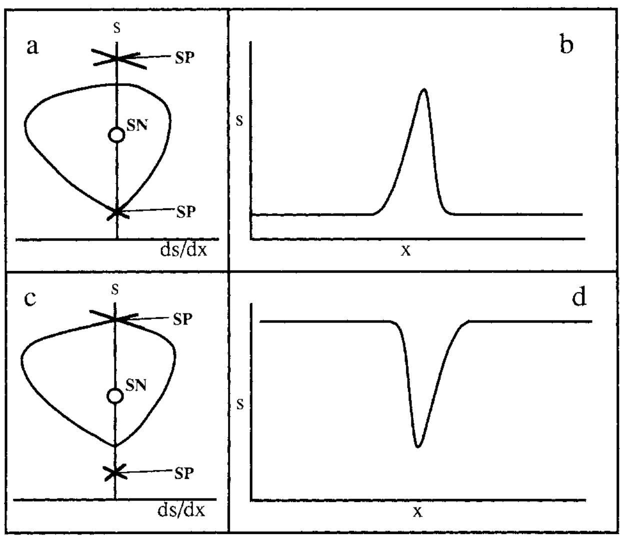

Figure 6. Solitary waves.

Collision of one saddle and a limit cycle results in a solitary wave with a long segment of uniform saturation on both sides. Limit cycles surround the spiral focus (SN) and can collide with saddle points at lower saturation (a, b) or at higher saturation (c, d).

so that a homoclinic connection occurs. Fixed points are obtained as solutions to Eqs. 50 and 51 at the fixed values of the parameters. If one of the parameters is varied slightly, the limiting condition shown in Figure 6a will change to possess either no closed orbits or a limit cycle in the form of a closed loop surrounding the spiral focus and lying entirely between the two saddle points. The saturation profile of a limit cycle very near the connection conditions takes the form of a solitary moving region of nonuniform saturation, surrounded by a very long segment of uniform flow corresponding to the saddle fixed point (see Figure 6b). The average flow through such a solitary wave is essentially the same as the flow for the uniform state corresponding to the saddle fixed point.

There are two distinct type of solitary waves in the present model: those which have saturation higher than the surrounding uniform flow, as shown in Figures 6a and 6b, and those which have lower saturation as shown in Figures 6c and 6d. A comparison of Figures 6a or 6b with Figures 6c or 6d readily differentiates these two types of solitary waves. For the liquid flux and U_T specifications corresponding to a solitary wave solution, one can certainly find a truly uniform state by solving the steady-state equations of motion. The stability of this uniform state (within the framework of the 1-D model) can also be examined using the criterion derived earlier (Eq. 34). An interesting feature is that, for certain flow conditions, this uniform state has been found to be stable! In other words, for some flow conditions, both stable uniform flow and high-amplitude nearly-solitary wave solutions exist!

Double heteroclinic connections

Another type of global bifurcation occurs when a limit cycle collides simultaneously with saddle points on both upper and lower branches. In the parameter space plot of Figure 5, the homoclinic connections emanating from the double-zero point at low wave speed represent connections with lower-branch saddles, while the curve from the higher wave speed double-zero point are connections with upper branch saddles. These two curves intersect at a single point, called the double heteroclinic connection. A representation of a double heteroclinic connection in phase space is shown in Figure 7. In the x coordinate, the saturation spends a long time at one saddle and then quickly, but not instantaneously, jumps to the lower saddle, spends a long time there, then jumps back, and so on.

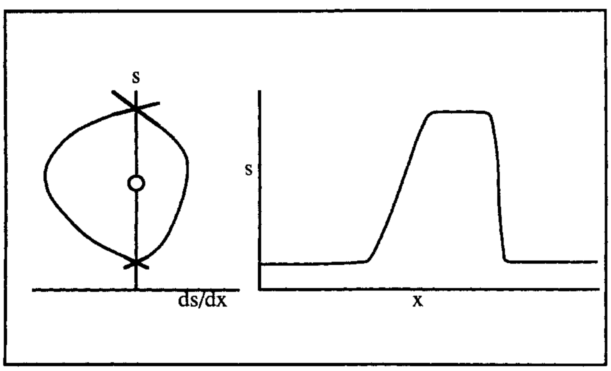

Figure 7. Double heteroclinic connection.

Double heteroclinic connections involve simultaneous collision of limit cycles with two saddle fixed points (a) and result in a "square" waveform with two plateaus (b).

The amount of time spent near each saddle point by limit cycles which are almost double heteroclinic connections depends on their location in parameter space relative to the connection conditions. Clearly, such limit cycles can have average fluxes of the two phases which span a range between connection with the upper saddle only as in Figure 6c, to connection with the lower saddle only as in Figure 6a. As shown in Figure 2, the periodic solution branches for several constant average flux conditions all approach the double heteroclinic connection point along different paths.

For the total flux U_T used in Figure 2, the uniform flow conditions corresponding to both the upper and lower saddle fixed points would be stable in the 1-D analysis. This implies that some operating conditions with stable uniform solutions also possess high-amplitude periodic solutions near the double heteroclinic point!

Stability of the periodic branch

Figure 8 shows curves for the same average flux conditions as shown in Figure 2, but plots saturation amplitude vs. wave number ω. All curves start from zero amplitude at the critical wave number and decrease in wave number as they grow. The curves reach constant amplitude, but continue toward zero wave number. This portion of the curves results from proximity to the double heteroclinic connection. From the shape of the curves, the Hopf bifurcation is evidently supercritical in ω, and the resulting periodic solutions are stable to periodic perturbations of the same total spatial period consistent with the boundary conditions in the 1-D model. These same branches of periodic solutions can be generated directly as traveling wave solutions to the discretized partial differential equations. They do have the inferred stability properties for the cases we have analyzed, when the total wavelength is constrained to a single period of the traveling wave solutions. There are indications that bifurcations

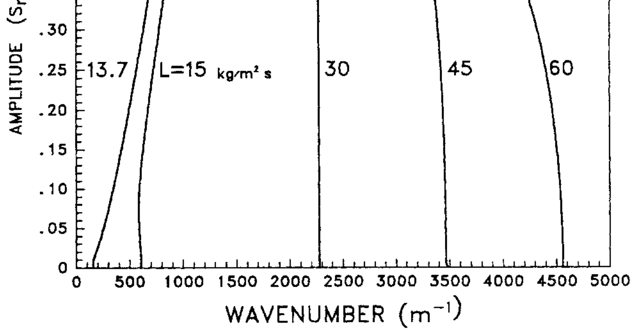

Figure 8. Amplitude vs. wave number.

Curves of Figure 2 are shown here in terms of wave number and amplitude. High-amplitude solutions approach constant amplitude at zero wave number due to proximity to the double heteroclinic connection.

to more complicated (e.g., quasiperiodic) solutions may exist for some combinations of average fluxes. In the following discussion, we shall refer to stability in the constrained sense only.

As a critical wave number approaches zero (the 1-D stability transition), the amplitude curves tend to swing to larger wave number before approaching the heteroclinic connection. This has already begun for the $L = 15$ curve in Figure 8. The periodic solutions along the outward-going lower part of the branch (having a positive slope in Figure 8) are unstable in the 1-D model with periodic boundary conditions. At the double-zero singularity, the critical wave number is zero and the periodic branch becomes attached to the $\omega = 0$ axis at two points. As the ratio of liquid flux to total flux is varied past the stability transition and into the stable uniform flow regime, the double heteroclinic connection and the nearby solutions persist at high amplitude. At lower amplitude, the other end of the branch of periodic solutions detaches from the steady flow solutions. The lower, unstable part of the branch now terminates at $\omega = 0$ on a solitary wave solution.

Infinite-Wavelength Endpoint Analysis

From the above discussion of the stability of traveling waves in the 1-D model, we can conclude that solutions corresponding to parameter values near a double heteroclinic connection are stable solutions to the full model when restricted to one dimension and periodic boundary conditions. Let us now return to the original constrained wave problem, in which the average liquid flux constraint is included (Eq. 69). As already discussed, there is only one free parameter in such a model, either the wave speed or, equivalently, the wavelength. This permits an infinite number of fully-developed, periodic traveling wave solutions. We have no way of choosing the preferred wavelength from this type of analysis, but experimental observations suggest that pulse lengths are much greater than those corresponding to the critical wave number.

Periodic solutions having physically relevant wavelength (greater than the packing size) lie very close to global bifurcations and have similar amplitude and speed. This may be seen quite readily in Figure 2, where the segments of trajectories for which the computed wavelength is larger than the size of the packing particles are shown as solid lines. Thus, the dotted-line segments are certainly not physically relevant. The wavelength increases rapidly on the solid-line segment of each trajectory and becomes infinite as the double heteroclinic connection point is reached. Physically-relevant pulses having wavelengths of at least tens of particle diameter are indistinguishable from this infinite wavelength point in Figure 2. This suggests that we focus our attention on the infinite-period bifurcations. By calculating the wave speed and relative liquid flux at which such a singularity occurs in the traveling wave model, we can identify properties of the time-dependent flow which occurs at a particular total volumetric flux.

Periodic regime map from the model

For given average fluxes L and U_T, the traveling wave analysis introduced a free parameter. When we restrict our attention to infinite-wavelength bifurcations, however, this free parameter (the wave speed) is uniquely determined and it emerges as part of the solution, depending only upon the physical flow parameters. Then, a map of the time-dependent regime can be constructed from knowledge of the location of 1-D stability transitions and fluxes associated with the upper and lower plateaus of the double heteroclinic connection over a range of U_T values.

It is possible to calculate the location of the homoclinic and double heteroclinic points directly, without following a branch of constant flux solutions from a Hopf Bifurcation for each total volume flux of interest (Kevrekidis, 1987), i.e., without generating the full details in Figure 5 for each value of U_T. This procedure is described in more detail in Appendix C. Once the location of one such singularity is known, numerical continuation techniques (e.g., AUTO 86, Doedel, 1986) can be employed to find the location and properties at other parameter values. The essential properties of interest are the wave speed and the saturation of the two steady flow solutions which form the upper and lower plateau regions of the resulting square wave.

Figure 9 shows such a regime map, plotting the ratio of average liquid superficial velocity to total (U_L/U_T) vs. the total superficial velocity. The ordinate of this map can be understood as the fraction of the volumetric flow due to the liquid phase. The lower boundary of the map corresponds to all gas flow, while the upper boundary corresponds to all liquid flow.

The 1-D stability transitions are indicated by the solid curve. Points to the left of this curve possess stable uniform flow solutions, while the uniform flow is unstable for points inside the curve. The dashed curve corresponds to the upper and lower plateaus of the double heteroclinic connection. Points within the dashed curve possess high-amplitude "square wave" periodic solutions. The points in region B have unstable uniform flow, but do not exhibit square-wave behavior at high amplitude. These points, however, do have high-amplitude long-wavelength solutions which take the form of solitary waves.

Periodic branch in each region

The regime map in Figure 9 can be subdivided into six regions which have qualitatively different families of periodic solutions.

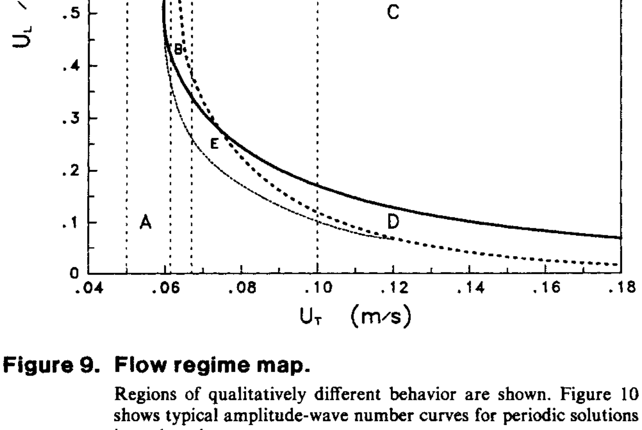

Figure 9. Flow regime map.

Regions of qualitatively different behavior are shown. Figure 10 shows typical amplitude-wave number curves for periodic solutions in each region.

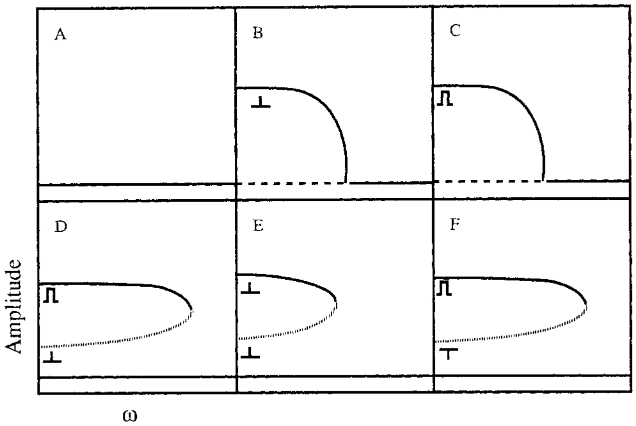

Figure 10. Characteristics of periodic solution branches.
The variation in amplitude with wave number of the periodic branch is shown schematically here for each region indicated in Figure 9.

Figure 10 shows schematically how the periodic solutions in each region vary with wave number.

Region A contains points which have *stable uniform steady flow,* and no time-dependent solutions.

In region B, lying in the regime of unstable uniform steady flow, but outside the double heteroclinic plateau curve, one obtains stable *high-amplitude solitary waves* at zero wavenumber. The branch of periodic solutions for region B extends from zero amplitude at the critical wave number to a high-amplitude solitary wave of the type shown in Figures 6a and 6b at zero wave number. The amplitude and speed of these solitary waves is dependent on the location of the point within the region.

In region C, the double heteroclinic connection dominates the high-amplitude behavior, and one obtains *stable square waves* at zero wave number. The solitary waves of region B have collided with the upper (saddle) uniform solution, and the wave speed and amplitude of the resulting square waves depend only on the total superficial velocity. The width ratio between upper and lower plateaus is determined by the relative amounts of liquid and gas fluxes.

In region F, one obtains *a stable uniform steady flow and also a stable square-wave solution* at zero wavenumber. The periodic solutions do not extend to zero amplitude. Instead, a low-amplitude solitary wave (of the type shown in Figures 6c and 6d) has appeared, with an associated set of unstable period solutions. These extend to higher wave numbers and undergo a turning point. The upper part of the periodic branch is stable and terminates at zero wave number in a square wave. The solitary wave is one with a traveling region of lower saturation than the surrounding flow. At the border between regions F and A, the period branch collapses onto itself and disappears.

Region D is similar to Region F, except that the low-amplitude unstable solitary waves have higher saturation than the surrounding uniform flow, as in Figures 6a and 6b. The squares waves in this region will also have narrower high-saturation plateaus relative to those in region F.

In region E, one obtains *a stable uniform steady flow, a stable high-amplitude solitary wave solution, and also an unstable solitary wave with lower amplitude* at zero wavenumber. The bifurcation pattern is similar to those in regions D and F. In this region the higher amplitude part of the periodic branch terminates not in a square wave, but in another solitary wave which also has different wave speed from the low-amplitude solitary wave. The size of this region is exaggerated in Figure 9. Movement from regions D or E into region A will result in disappearance of the periodic branch.

In a narrow part of region C, near its boundary with region B, the lower plateau of the square wave solution corresponds to an *unstable* uniform solution. It is in this small region that bifurcations to quasiperiodic solutions can occur in the partial differential equations as discussed in appendix B. This is consistent with the observations of pulses with multiple frequency reported by Sato et al. (1973).

Infinite-wavelength bifurcation diagrams

The transitions from one region to another in Figures 9 and 10 can be better elucidated by construction of one-parameter bifurcation diagrams for solutions at zero wave number in terms of the U_L/U_T (flow fraction liquid) parameter. Four qualitatively distinct diagrams can be made depending on the number and type of regions involved. Representative cuts at constant total superficial velocity are shown in Figure 9 as the vertical lines labeled I-IV. Figure 11 shows schematically the amplitude of the zero wave number solutions as U_L/U_T is varied from 0 to 1 along the representative cuts.

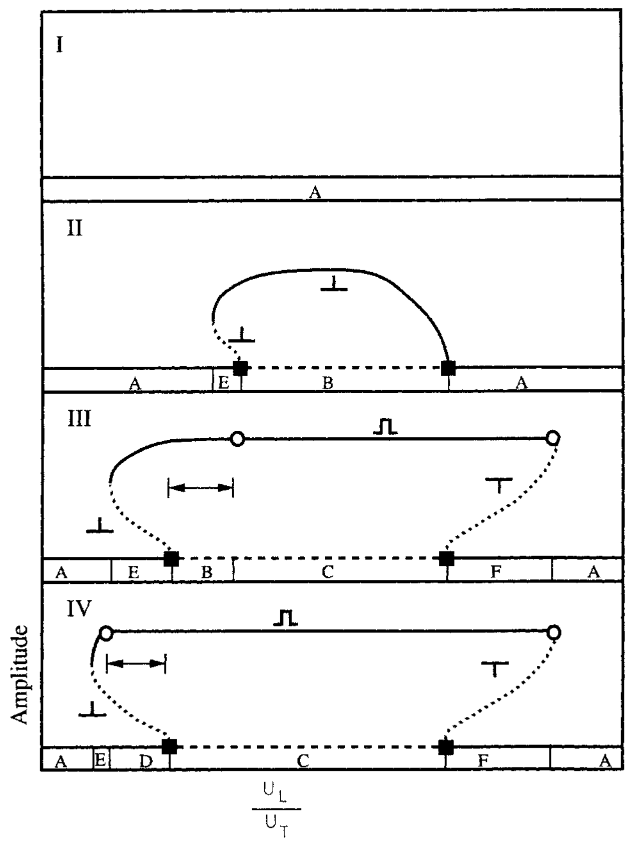

Figure 11. Zero wave number bifurcation diagrams.
Variation in amplitude and stability of the infinite period solutions as the flow fraction liquid is varied along the vertical cuts in Figure 9.

Cut I lies entirely in region A. The uniform steady-flow solution at zero amplitude is stable over the entire range, and no periodic solutions exist.

Cut II passes in order through regions A, E, B, and A. The bifurcation diagram shows stable uniform flow for all points up to the stability transition curve at the E-B boundary. At this point, the lower branch of solitary waves emerges from the uniform solution. At the A-E boundary, the solitary waves undergo a turning point, leaving no periodic solutions in region A, and two solitary wave solutions in region E. On the other side of the E-B boundary, there is only one solitary wave solution, and this recedes supercritically back into the uniform steady solution as the B-A boundary is crossed.

Cut III is similar to cut II, but now the solitary waves created from the E-B stability transition undergo a global bifurcation to a square wave as the B-C boundary is crossed. These square waves persist at constant amplitude up to the F-A boundary, where another global bifurcation occurs. This time the solitary waves have lower saturation than their saddle point (as in Figures 6c and 6d). These solitary waves immediately undergo a turning point and recede subcritically into the second stability transition at the C-F boundary.

Cut IV is similar to cut III, except that the solitary waves change to square waves before the first Hopf bifurcation. Now the square waves are present over the entire range of unstable uniform flows.

Practical Implications

Trickling-to-pulsing transition

Grosser et al. (1988) concluded that the uniform-flow stability transition curve in Figure 9 represents the onset of the pulsing flow regime. In the light of the results just presented, this conclusion should be modified. Some of the points which have unstable uniform flow may not be capable of supporting large, observable pulses. In region B, for example, high-amplitude solutions are similar to the solitary wave solution. While such nearly solitary waves do have very long wavelength, the actual size of the region of perturbed saturation is very small, of the order of the packing size for the properties used here. The nearly square wave solutions, however, can produce pulses of any width. *Thus observable pulsing flow is predicted only in those regions of the regime map (D, E, and F) which have square wave solutions at zero wavenumber.*

In region B, the uniform flow is unstable, but time-dependent solutions do not correspond to wide regions of high liquid holdup. Instead, the time-dependent solutions take the form of narrow fluctuations from uniform flow. This may be identified with *a transition region* reported by some experimental investigators (Weekman, 1964; Beimesch and Kessler, 1971; Sato et al. (1973), which appears visually as a rippling in the uniform-flow pattern.

If we now examine bifurcation cut IV in Figure 10, we can imagine an experiment where U_L/U_T is raised gradually, assuming that the long-wavelength solutions will be observed. The uniform steady flow will remain stable until the first stability transition at the D-C boundary is reached, after which the nearly square waves become the stable solutions and pulsing flow ensues. If we now decrease the flow fraction liquid, the stable high-amplitude square waves can persist until the E-D boundary is crossed, whereupon the stable uniform flow returns. In short, *the model predicts a hysteresis in the trickling-pulsing transition.* Such a hysteresis has indeed been observed experimentally, but has not been studied closely. The model also predicts a sudden change from uniform steady flow to high-amplitude time-dependent flow as the transition occurs.

Pulse properties

There are several conclusions that can be drawn from the present analysis in one dimension. First, the total superficial velocity is a natural parameter for correlating the properties of one-dimensional time-dependent flow. If we consider pulsing flow to exist where the double heteroclinic "square-wave" solutions are possible, then the properties of an individual pulse are dictated by those of the double heteroclinic connection, which depend only on the total superficial velocity and not the distribution of flow between the two phases. This implies that pulse speed and amplitude should be functions of only U_T for one-dimensional, fully-developed pulses.

Wave Speed. We can compare the predicted wave speed from the model with experimentally measured pulse speeds in a bed with similar packing and fluids. Such experimental measurements were reported by Rao and Drinkenberg (1983) in the form of a correlation for the variation of pulse speed with average interstitial gas velocity. The accuracy of the correlation was given as ±5%. Unfortunately, we could not report their results with total superficial velocity as the abscissa. In Figure 12, the range of velocity predicted by that correlation is compared to the wave speed at the double heteroclinic connection predicted by the model. Since the average gas velocity also depends on the distribution of flow between liquid and gas, we have plotted the interstitial gas velocity in the gas-rich, low-saturation plateau. As shown in the figure, there is reasonable agreement in the slope and magnitude of the two curves at low gas velocity.

Close examination of the location of the double heteroclinic connections reveals that they must exhibit negative relative gas flux ($k_g < 0$). This implies that one-dimensional pulses will always travel slightly faster than the interstitial gas velocity ($c < \mu_g$). Rao and Drinkenberg (1983) observed that pulses which formed at low gas velocity do travel at nearly the same speed as the gas phase. Thus, a one-dimensional analysis is

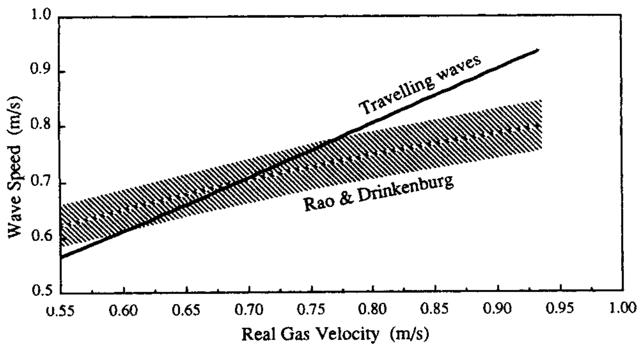

Figure 12. Comparison of predicted and observed wave velocities.

Narrow line is prediction based on speed of square waves. Shaded region represents Rao and Drinkenberg (1983) empirical correlation.

reasonable at low gas velocities. The agreement between the model predictions and experimental data is remarkable, considering that no adjustable parameters were used.

At high gas velocities, the experimental correlation shows much lower pulse speeds than the model predicts. It is a common observation in the literature that, at higher gas velocities, the pulses travel much slower than the gas, contrary to our predictions. However, as mentioned in the introduction, the pulses observed experimentally at those conditions are not one-dimensional (e.g., Weekman and Myers, 1964).

Holdup Levels. It is also possible to compare the saturation levels in the plateaus of the square wave solutions with the experimentally-measured holdup levels for the liquid- and gas-rich parts of a pulse. The one-dimensional model predicts that the holdup in the liquid-rich part of the pulse will increase as total superficial velocity is increased. Likewise, the holdup of the gas-rich part will decrease. At very high total superficial velocity, the model would predict liquid-full pulses, with residual liquid saturation prevailing in-between. The experiments of Rao and Drinkenberg (1983) and Beimesch and Kessler (1971) agree with the model in the gas-rich portion, showing decreasing liquid holdup in that region with increase in gas velocity. Beimesch and Kessler also found that, at high gas velocity, the saturation in the gas-rich part approached the residual liquid saturation. In the liquid-rich part, however, they both observed a decrease in the saturation as gas velocity was increased. This discrepancy can again be related to the two-dimensional structure of the actual pulses at high gas velocity. The measured saturation was the average over the entire cross-section.

Pulse Frequency. The analysis of one-dimensional, fully-developed periodic behavior indicates that a continuum of wavelengths and frequencies can be supported by the bed. There appears to be no intrinsic pulse frequency. Indeed, while many investigators report values for pulse frequency, the actual frequency observed can vary by 20% over the course of a single experiment, and pulses can appear in doublets and triplets (Rao and Drinkenberg, 1983). The pulse speed, however, varies by less than 5%. Our results support the conclusion that pulse frequency in a finite bed is determined by the conditions at the point of pulse inception. The proximity of the high-amplitude solutions to the infinite period bifurcations suggests that small variations in the conditions at the inception point could lead to large fluctuations in the eventual wavelength, but not the wave velocity. Thus, it is unrealistic to expect the model to predict pulse frequencies.

Discussion

Persistence of qualitative features

The above presentation shows the structure of the time-dependent regime of the model for particular bed and fluid properties and for certain constitutive relations for drag forces, deviatoric stress, and capillary pressure. These were chosen to be as realistic as possible in the prediction of the properties of uniform steady flow so that comparisons could be made with experimental observations. It is important to note that the main features of the time-dependent regime, i.e., the nature of the stability transitions and the dominance of certain global bifurcations, are not dependent on any of these choices. We have performed a sensitivity analysis of the effect on these features of both qualitative and quantitative changes in the constitutive relations. We found that these features arise from the underlying structure of the equations of motion and are persistent over a wide range of bed and fluid properties and constitutive relations. Therefore, we can conclude that the *features described in this paper are robust.*

It is relatively unimportant how the drag force and other relations are derived and interpreted, as long as they are qualitively correct in the predicted trends. While some features of the constitutive relations we have employed may be questionable from a quantitative point of view and may lead to slightly more complicated behavior, the basic methods and results presented here are generally valid for any reasonable alternative relations.

Transition to higher dimensional solutions

Comparison of predicted "square-wave" pulse properties with experimental observations reveals discrepancies in the pulse velocity and the saturation of the liquid-rich part of the pulse. This can be attributed to the one-dimensional nature of the present analysis, while it is known that actual pulses at high flow rates are not one-dimensional. The present analysis remains valuable, however, since it provides a starting point for the development of a multidimensional analysis. The one-dimensional traveling waves are also solutions to the two- and three-dimensional model. A 2-D linear stability analysis predicts the same transition from uniform steady flow to one-dimensional traveling waves. It is likely that multidimensional solutions will bifurcate from these unidimensional waves as the severity of the flow is increased.

Critical wave number and capillary forces

In previous papers (Grosser et al., 1988; Dankworth and Sundaresan, 1989), the change in stability of the uniform state was attributed to a competition between the inertial forces and the capillary forces in the bed. Inertial forces tend to destabilize, while the capillary forces tend to stabilize the uniform flow. In the present analysis of the unstable regime, that competition again appears in the stabilization of the uniform flow to high-frequency perturbations. The critical wave number at which stabilization occurs is such that only very small perturbations are stable, on a scale comparable to the particle size. The explanation for this lies in the effective range of the forces involved. In the unstable regime, the relatively weak capillary forces can only exert influence over a distance which scales with the particle size. Over larger distances, the inertial forces completely dominate. Thus it is reasonable to expect stabilization over length scales on the order of a single particle only. The magnitude of the critical wave number is suggestive of the opening and closing of a single pore. It is intresting to observe that the model may in this way indirectly account for pore-scale bridging and blockage.

Summary

The objective of this paper was to show how the model of Grosser et al. (1988) can be extended to describe not only the transition to pulsing flow, but also the nature of fully-developed pulsing. In order to begin such an analysis, it was necessary to propose a constitutive relation for the viscous and pseudoturbulence stresses which provides dissipation of high-frequency disturbances and renders the model well posed.

Having proposed a well-posed closure scheme for the equations of motion, we then proceeded to examine the model for wavelike solutions. By postulating that such solutions will travel at constant speed, a change of variables was made which reduced the partial differential equations to a single, nonlinear, second-order ordinary differential equation. This traveling wave equation was then analyzed using the tools of bifurcation and singularity theory to describe the qualitative nature of traveling wave solutions. Limit cycles of this ODE can be identified with fully-developed periodic solutions of the full partial-differential equations.

The 1-D wave solutions to the model can exist over a wide range of wavelengths. At realistically long wavelength and high amplitude, however, these solutions have the shape of either a solitary wave or a square-wave oscillation between two spatially uniform flows. The upper and lower saturation plateaus of the long-period square waves were uniform solutions of the equation which have the same total volumetric flux, but different proportions of liquid and gas flux. Analysis revealed that these periodic solutions lie very near a double heteroclinic connection between two saddle-type fixed points in the traveling wave frame. By numerically following the infinite-period bifurcations in the model, we constructed an operating diagram or regime map which separates the space of external flow conditions into regions having qualitatively similar hydrodynamic behavior.

Comparison of these one-dimensional waves to experimentally determined properties of pulsing flow suggests that while the predicted wave speed and saturation levels agree with experiment for conditions close to the trickling-pulsing transition, these predictions diverge from reality for fluxes far from the transition. We note that several investigators (Beimesch and Kessler, 1971; Weekman and Myers, 1964; Christensen et al., 1986) have observed two- and three-dimensional pulse shapes, which the one-dimensional form of the model cannot simulate. The model also predicts a hysteresis in the trickling-to-pulsing transition, which has not been studied closely in the literature.

Acknowledgment

This work was supported by the Fannie and John Hertz Foundation in the form of a graduate fellowship awarded to D. C. Dankworth, the National Science Foundation under grant NSF EET 87-17787 and a Packard Foundation Fellowship.

Notation

A, B = Ergun constants
A_1 = see Eq. 48
c = wave speed
c_{HB} = wave speed at a Hopf bifurcation
c_{LP} = wave speed at a limit point
C_1, C_2, C_3 = coefficients of the stability criterion, Eqs. 35–37
d_e = particle diameter
e = deviation of the liquid volume fraction from uniform
$\underline{\underline{E}}$ = combined stress tensor
Eo^* = Eotvos number, Eq. 7
F = see Eq. 49
$\underline{F}_i, i = l, ig$ = total drag force per unit bed volume experienced by phase i
$F_{iz}, i = l, g$ = drag force per unit bed volume experienced by phase i in the axial direction
g = acceleration due to gravity
G = gas-phase mass flux
j = square root of -1
$J(\epsilon_l)$ = Leverett J-function
$J'(\epsilon_l)$ = $dJ/d\epsilon_l$
k = permeability of the packed column $(\epsilon/k)^{1/2} = A^{1/2}(1-\epsilon)/\epsilon d_e$
k_i = mass fluxes relative to the traveling frame
L = liquid-phase mass flux
$p_i, i = l, g$ = pressure in phase i
p_c = capillary pressure
$\underline{\underline{R}}_i, i = l, g$ = pseudoturbulence stress tensor for phase i
s_l = ϵ_l/ϵ, liquid saturation
t = time
$u_i, i = l, g$ = local mean velocity of phase i
U_L = superficial velocity of the liquid phase
U_T = combined superficial velocity of liquid and gas phases
$W_1 - W_7$ = see Eqs. 25–31
$\overline{W}_4$ = see Eq. 46
$\overline{W}_7$ = see Eq. 47
x = traveling coordinate
y = symbol for a state variable in Eq. 23
z = axial distance

Greek letters

$\alpha_{ij}, \beta_i, ij = l, g$ = see Eq. 23
ϵ = porosity of the bed
$\epsilon_i, i = l, g$ = volume fraction of phase i in the bed
ϵ_l^r = residual or static liquid holdup
λ_i^* = effective bulk viscosity
λ = length scale, wavelength
λ_{HB} = period of initial limit cycles at a Hopf bifurcation
$\rho_i, i = l, g$ = density of phase i
$\mu_i, i = l, g$ = viscosity of phase i
μ_i^* = effective shear viscosity
$\overline{\mu}_i$ = effective combined viscosity
σ = interfacial tension
$\underline{\underline{\tau}}_i, i = l, g$ = viscous stress tensor for phase i
ω = wave number of imposed disturbance
ω_c, ω_{HB} = critical wave number for zero growth
ξ = real part of the complex growth rate
υ = imaginary part of the complex growth rate
χ = complex growth rate

Superscript

o = uniform steady state

Literature Cited

Anderson, T. B., and R. Jackson "A Fluid Mechanical Description of Fluidised Beds; Stability of the state of uniform fluidisation," *Ind. Eng. Chem. Fund.*, **7**, 12 (1968).

Christensen, G., S. J. McGovern, and S. Sundaresan, "Cocurrent Downflow of Air and Water in a Two-Dimensional Packed Column," *AIChE J.*, **32**, 1677 (1986).

Dankworth, D. C., and S. Sundaresan, "A Macroscopic Model for Countercurrent Gas-Liquid Flow in Packed Beds," *AIChE J.*, **35**, 1282 (1989).

Doedel, E. J., "AUTO, A Program for the Automatic Bifurcation Analysis of Autonomous Systems," *Cong. Num.*, **30**, 265 (1981); *AUTO 86 User Manual*, Pasadena (1986).

Grosser, K. A., R. G. Carbonell, and S. Sundaresan, "The Transition to Pulsing Flow in Trickle Beds," *AIChE J.*, **34**, 1850 (1988).

Guckenheimer, J., and P. Holmes, Nonlinear Oscillations, Dynamical Systems, and Bifurcations of Vector Fields, *Applied Mathematical Sciences*, Vol. 42, Springer-Verlag (1983).

Homsy, G. M., M. M. El-Kaissy, and A. K. Didwania, "Instability Waves and Origin of Bubbles in Fluidized Beds," *Int. J. Multiphase Flow*, **6**, 305 (1980).

Kevrekidis, I. G., "A Numerical Study of Global Bifurcations in Chemical Dynamics," *AIChE J.*, **33**, 1850 (1987).

Leverett, M. C., "Capillary Behavior in Porous Solids," *Trans. AIME*, **142**, 159 (1941).

Melli, T., "Two-Phase Cocurrent Downflow in Packed-Beds: Macroscale from Microscale," PhD Thesis, Univ. Minnesota (1989).

Ng, K. M., "A Model for Flow Regime Transitions in Cocurrent Downflow Trickle-Bed Reactors," *AIChE J.*, **32**, 115 (1986).

Rao, V. G., and A. A. H. Drinkenberg, "Pressure Drop and Hydrodynamic Properties of Pulses in Two-Phase Gas-Liquid Downflow through Packed Columns," *Can. Chem. Eng. J.*, **62**, 158 (1983).

Saez, A. E., and R. G. Carbonell, "Hydrodynamic Parameters for Gas-Liquid Cocurrent Flow in Packed Beds," *AIChE J.*, **31**, 52 (1985).
Satterfield, C. N., "Trickle Bed Reactors," *AIChE J.*, **21**, 209 (1975).
Sato, Y., T. Hirose, F. Takahashi, M. Toda, and Y. Hashiguchi, "Flow Pattern and Pulsation Properties of Cocurrent Gas-Liquid Downflow in Packed Beds," *J. Chem. Eng. Japan*, **6**, 315 (1973).
Sundaresan, S., "Mathematical Modeling of Pulsing Flow in Large Trickle Beds," *AIChE J.*, **33**, 455 (1987).
Weekman, V. W., and J. E. Myers, "Fluid Flow Characteristics of Cocurrent Gas-Liquid Flow in Packed beds," *AIChE J.*, **10**, 951 (1964).

Appendix A: Multiple Fixed Points in the Traveling Wave Frame

In the cocurrent downflow regime, only one uniform steady-flow solution exists for each value of liquid and gas mass flux. Transformation to traveling wave coordinates, however, allows the presence of multiple steady-flow solutions, since only the total volume flux is held constant. This is demonstrated in Figure A1.

At any point in the bed, gas and liquid fluxes are related by the total volume flux equation (Eq. 17). This means that fluxes in the bed must lie along a line in *L-G* space. At every point along this *L-G* line, there is a value of liquid saturation and velocity which satisfies the uniform state equation $F = 0$. This uniform liquid saturation is plotted vs. liquid flux in Figure A1. The bed will not necessarily satisfy the uniform flow conditions at every point. However, there is a relation between the saturation and interstitial velocity, Eq. 43, which is satisfied at every point. This relationship is indicated by the dashed line in Figure A1. The line has slope $1/c$ and intercept $-k_l/c$. Points of intersection between this line and the uniform state saturation curve are fixed points of the traveling wave equation. It is easy to see that by adjusting the slope and intercept (by changing c, k_l) there can be one, two or three intersections. Note that the uniform saturation curve ends abruptly at $s = s^r$, and $s = 1.0$. Evaporation of the fixed points occurs as the mass balance line crosses one of the ends of the curve.

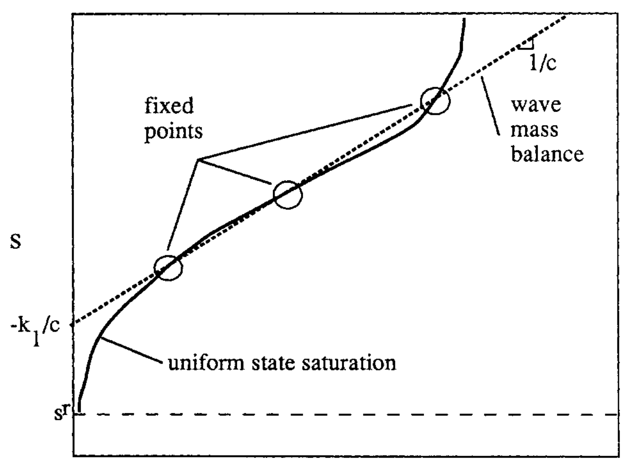

Figure A1. Graphical interpretation of multiple fixed points in the traveling wave model.

Appendix B: Spectral Integration of PDE

Pseudo spectral method

In order to examine the relation between the traveling wave results and the behavior of the full 1-D model in the unstable flow regime, a pseudospectral discretization of the 1-D model was analyzed numerically. For this analysis, the equations of motion were combined to form two partial differential equations for the liquid saturation and the local mean liquid interstitial velocity:

$$\frac{\partial s}{\partial t} = - s\frac{\partial u_l}{\partial z} - u_l\frac{\partial s}{\partial z} \tag{B1}$$

$$\begin{aligned}(\epsilon_g \rho_l + \epsilon_l \rho_g)\frac{\partial u_l}{\partial t} = {} & \frac{\partial^2 u_l}{\partial z^2}[\epsilon_g \bar{\mu}_l + \epsilon_l \bar{\mu}_g] \\ & - \frac{\partial u_l}{\partial z}[\epsilon_g \rho_l u_l - \epsilon_l \rho_g u_g] \\ & + \frac{\partial u_l}{\partial z}\frac{\partial \epsilon_l}{\partial z}\left[2\bar{\mu}_g\left(1 + \frac{\epsilon_l}{\epsilon_g}\right)\right] \\ & + \frac{\partial \epsilon_l}{\partial z}[\rho_g u_g^2 - \rho_g u_g u_l + \epsilon_g p_c'] \\ & + \frac{\partial \epsilon_l}{\partial t}\rho_g [u_g - u_l] \\ & + \frac{\partial^2 \epsilon_l}{\partial z^2}\bar{\mu}_g [u_l - u_g] \\ & + \left(\frac{\partial \epsilon_l}{\partial z}\right)^2\left[\frac{2\bar{\mu}_g}{\epsilon_g}(u_l - u_g)\right] \\ & + \epsilon_g g(\rho_l - \rho_g) + \frac{\epsilon_g}{\epsilon_l}F_l - F_g\end{aligned} \tag{B2}$$

where the gas-phase interstitial velocity is given by the expression for conservation of total volume flux as:

$$u_g = \frac{U_T - u_l \epsilon_l}{\epsilon - \epsilon_l} \tag{B3}$$

In this case, we are interested in possible periodic or quasiperiodic behavior in a very long bed. To do this, we specify a wavelength and search for periodic solutions having that wavelength. The constant average flux condition can be directly incorporated into the discretization.

In the discretized equations, the wavelength or box size is now a natural parameter to be varied in search of stability changes. Variation in wavelength corresponds to variation in the minimum wave number of resulting solutions. We expect from the linear stability analysis of the 1-D model that the uniform flow solution will be stable for wave numbers greater than the critical wave number and that there will be a Hopf bifurcation, and subsequent birth of periodic traveling wave solutions as the wave number passes through the critical value. A bifurcation analysis of the discretized equations using AUTO (Doedel, 1986) exhibits the predicted behavior. At the box size corresponding to the critical wave number, the uniform state becomes unstable, and a branch of periodic, limit cycle solutions can be found to emanate from the change in stability. These periodic solutions can be continued to higher amplitudes and are identical to the branch of traveling waves found for the same average fluxes.

The speed of the waves is given by the ratio of the box size to their period.

Other Hopf bifurcations from the uniform solution occur at integer multiples of the critical box size. Branches of periodic solutions (traveling waves) emanate from these secondary Hopf bifurcations also. These periodic solutions have the same shape as the original branch, but with the waveform repeated in the spatial dimension.

The stability of the periodic solutions is easily determined by examination of the Floquet multipliers of the limit cycles of the discretized system. As expected, the stability of the limit cycles follows the usual rules for a branch of periodic solutions emerging from a Hopf bifurcation. For the cases we investigated far from the transition region of the regime map, we did not observe any further bifurcations of the traveling wave branches. In the transition area between regions B an C in Figure 9, however, we have seen preliminary evidence for period doubling and Hopf bifurcations along the secondary branches of periodic traveling wave solutions. This implies that, in this region, stable quasiperiodic time-dependent solutions may exist.

Appendix C: Method for Direct Calculation of Saddle Connections

It is possible to calculate the location of the homoclinic and double heteroclinic points directly, without following a branch of constant flux solutions from a Hopf Bifurcation for each total volume flux of interest. Kevrekidis (1987) discusses methods for numerically locating homoclinic and single heteroclinic connections. We have developed an extension of those methods for converging accurately on double heteroclinic connections. The method involves location of the two saddle-type fixed points, and evaluation of the distance between the manifolds of the saddles on both sides. These distances can be used as an objective function. Standard numerical techniques can then be employed to converge on values of both c and k_l at which the distances between manifolds are zero. The variation of the location and properties of the double heteroclinic connection can then be studied by continuation in a third parameter, such as U_T.

Manuscript received Dec. 19, 1989.